Fatigue Fract. Engng Mater. Struct. Vol. 15, No. 2, pp. 187–202, 1992
Printed in Great Britain

8756-758X/92 $5.00 + 0.00
Fatigue of Engineering Materials Ltd

CRACK TIP BEHAVIOUR AND CRACK PROPAGATION IN DUCTILE MATERIALS

G. C. Li, H. Q. Liu, M. L. Du, Y. S. Hong and X. Zhang
Institute of Mechanics, Academia Sinica, Beijing 100080, People's Republic of China

(Received in final form 3 May 1991)

Abstract—Dilatational plastic equations, which can include the effects of ductile damage, are derived based on the equivalency in expressions for dissipated plastic work. Void damage developed internally at the large-strain stage is represented by an effective continuum being strain-softened and plastically dilated. Accumulation of this local damage leads to progressive failure in materials. With regard to this microstructural background, the constitutive parameters included for characterizing material behaviour have the sense of internal variables. They are not able to be determined explicitly by macroscopic testing but rather through computer simulation of experimental curves and data. Application of this constitutive model to mode-I cracking examples demonstrates that a huge strain concentration accompanied by a substantial drop of stress does occur near the crack tip. Eventually, crack propagation is simulated by using finite elements in computations. Two numerical examples show good accordance with experimental data. The whole procedure of study serves as a justification of the constitutive formulation proposed in the text.

NOMENCLATURE

τ^{ij} = Kirchhoff stress (contravariant tensor)
σ^{ij} = Cauchy (true) stress (contravariant tensor)
$D_{ij}^{(p)}$ = plastic deformation rate (covariant tensor)
σ_m = mean stress
$D_m^{(p)}$ = plastic mean deformation rate
σ_e = equivalent stress
$D_e^{(p)}$ = plastic equivalent deformation rate
D_e = total equivalent deformation rate
S_j^i = deviatoric stress (mixed tensor)
d_j^i = plastic deviatoric deformation rate (mixed tensor)

$$\epsilon_e^{(p)} = \int_0^t D_e^{(p)}\,dt$$

$$\epsilon_e = \int_0^t D_e\,dt$$

$$\epsilon_m^{(p)} = \int_0^t D_m^{(p)}\,dt$$

$$\frac{\mathcal{D}}{\mathcal{D}t} = \text{Jaumann rate}$$

g^{ij} = metric tensor
$E_{te}^{(p)}$ = deviatoric plastic tangent modulus
$E_{tm}^{(p)}$ = volumetric plastic tangent modulus
E = Young's modulus
ν = Poisson's ratio
$V_{i|j}$ = covariant derivative of velocity

INTRODUCTION

As a consequence of large plastic deformation and high triaxial tension, successive nucleation and growth of voids have been well examined and confirmed to be the main microstructural damage

that leads to final failure of ductile materials. Experimental reports, delivered by Hancock and Cowling[1], Beremin[2] and Xia *et al.*[3], lay solid ground to show that there are usually two generations of void nucleation involved in steels. Firstly large voids ($\sim 10\,\mu$m) around inclusions bonded weakly to the matrix are formed and can be taken as primary and initial voids. Afterwards secondary voids ($\sim 1\,\mu$m) surrounding fine precipitates of carbides, which have a strong interfacial bonding with the matrix, can be nucleated under higher stress/strain loading.

Numerical analyses by Li and Howard[4] and Li *et al.*[5] for modelling void damage have shown that the interaction between these two classes of voids can cause detrimental effects which are much worse than if the material were damaged only by single size voids distributed periodically. The plastic loading points distinguished by the same amount of void volume fraction can no longer trace the regular and smooth surfaces as those in Gurson's paper [6]. When secondary voids are progressively developed to a large extent, the overall elastic response of material is shown by Li[7] to greatly deteriorate. The normality and convexity rules then become questionable. The assumptions underlying the constitutive characterization based on Gurson's model and others are also discussed by Becker *et al.*[8]. They concluded that the key issues for improving the modelling capability should be the matrix material constitutive characterization, the improved quantification of void nucleation phenomena and non-uniform void distribution effects. These points are indeed closely related to the role played by the nucleation and growth of secondary voids in the matrix around primary voids.

Owing to these reasons, the prospective constitutive equations that can include the effect of ductile damage should be built on a more general basis. We therefore intend to employ in the present work, the equivalency in the expressions for the rate of dissipated plastic work. Based on microstructural studies, some criteria are proposed to predict the initiation of internal damage and final failure. A series of tests on axisymmetrically notched bars and smooth bars has been carried out previously, by Xia *et al.*[3] (in conjunction with computer simulations) and by Yang and Li[9], to determine the constitutive parameters involved in the equations and criteria.

Besides furnishing a theoretical framework to the constitutive equations, the main aim of the present study has been to assess the rationality and capability of those equations and criteria by applying them to modelling mode-I cracking problems. Two geometrical shapes of specimens were chosen for this purpose. Crack propagation was measured and compared with computational results. Distributions and evolution of stresses and strains in the region near the crack tip will be illustrated.

CONSTITUTIVE MODEL FOR DUCTILE MATERIALS

According to the definition given by Hill[10] for stress and strain to be conjugate, the rate of dissipated plastic work $\dot{W}_0^{(p)}$ under up-dated Lagrangian formulation, that is to say with respect to the configuration at some fixed generalized time t_0, should be expressed as

$$\dot{W}_0^{(p)} = \tau^{ij} D_{ij}^{(p)} = \tau_j^i D_i^{j(p)} \tag{1}$$

here τ^{ij} is the Kirchhoff stress which is related to the Cauchy (true) stress σ^{ij} by a definition as

$$\tau^{ij} = \frac{dv}{dv_0}\sigma^{ij} \tag{2}$$

here dv_0 and dv are respectively the initial and the deformed differential volume, corresponding to some fixed time t_0 and the current time t starting from t_0. The term $D_{ij}^{(p)}$ is the plastic part of the

deformation rate D_{ij}, which can be derived from the cavariant derivative of the velocity V_i by stating that

$$D_{ij} = \tfrac{1}{2}(V_{i|j} + V_{j|i}). \tag{3}$$

Both the Kirchhoff stress tensor τ_j^i and the plastic part of the deformation rate $D_i^{j(\mathrm{p})}$ can be resolved into their deviatoric and volumetric parts, correspondingly.

$$\tau_j^i = S_j^i + \delta_j^i(\tfrac{1}{3}\tau_k^k) \tag{4a}$$

$$D_i^{j(\mathrm{p})} = d_i^{j(\mathrm{p})} + \delta_i^j(\tfrac{1}{3}D_l^{l(\mathrm{p})}) \tag{4b}$$

and

$$S_j^i = \tau_j^i - \delta_j^i(\tfrac{1}{3}\tau_k^k)$$

$$d_i^{j(\mathrm{p})} = D_i^{j(\mathrm{p})} - \delta_i^j(\tfrac{1}{3}D_l^{l(\mathrm{p})}). \tag{5}$$

Substituting equations (4a) and (4b) into equation (1), we find

$$\dot{W}_0^{(\mathrm{p})} = S_j^i d_i^{j(\mathrm{p})} + \tfrac{1}{3}\tau_k^k D_l^l. \tag{6}$$

On the other hand, let us define

$$\dot{W}_0^{(\mathrm{p})} = \sigma_{\mathrm{e}} D_{\mathrm{e}}^{(\mathrm{p})} + 3\sigma_{\mathrm{m}} D_{\mathrm{m}}^{(\mathrm{p})}. \tag{7}$$

This expression denotes that the total rate of dissipated plastic work is obviously composed of two parts, one is done by the deviatoric components and the other belongs to the volumetric dissipation. It is easy to check that

$$\sigma_{\mathrm{m}} = \tfrac{1}{3}\tau_k^k \tag{8}$$

and

$$D_{\mathrm{m}}^{(\mathrm{p})} = \tfrac{1}{3}D_l^{l(\mathrm{p})} \tag{9}$$

represent the mean stress and the plastic mean deformation rate, respectively, in the volumetric part. We further nominate σ_{e} as the equivalent stress that has a definition of

$$\sigma_{\mathrm{e}} = (\tfrac{3}{2}S_j^i S_i^j)^{1/2} \tag{10}$$

and we call $D_{\mathrm{e}}^{(\mathrm{p})}$ the plastic equivalent deformation rate. Based on the need that equivalency must hold between equations (6) and (7) under whatever stress condition, with the equivalent stress being defined as equation (10), an immediate conclusion can be drawn as follows:

$$d_i^{j(\mathrm{p})} = \tfrac{3}{2}(D_{\mathrm{e}}^{(\mathrm{p})}/\sigma_{\mathrm{e}})S_i^j \tag{11}$$

and

$$d_j^{i(\mathrm{p})} d_i^{j(\mathrm{p})} = \tfrac{9}{4}(D_{\mathrm{e}}^{(\mathrm{p})2}/\sigma_{\mathrm{e}}^2)S_j^i S_i^j. \tag{12}$$

Then, consequently we should have

$$D_{\mathrm{e}}^{(\mathrm{p})} = (\tfrac{2}{3}d_j^{i(\mathrm{p})} d_i^{j(\mathrm{p})})^{1/2}. \tag{13}$$

This statement should not be taken as a definition but rather the consequence of the definition given for σ_{e} in equation (10), and it is also due to the equivalency of the expressions attributed to the deviatoric part of the dissipated plastic work rate in equations (6) and (7).

Substituting equation (11) into equation (4b), we have

$$D_j^{i(\mathrm{p})} = \frac{3}{2}\frac{D_{\mathrm{e}}^{(\mathrm{p})}}{\sigma_{\mathrm{e}}} S_j^i + \delta_j^i\left(\tfrac{1}{3} D_l^{l(\mathrm{p})}\right)$$

$$= \frac{3}{2}\frac{\mathscr{D}\sigma_{\mathrm{e}}/\mathscr{D}t}{E_{\mathrm{te}}^{(\mathrm{p})}\sigma_{\mathrm{e}}} S_j^i + \delta_j^i \frac{\mathscr{D}\tau_k^k/\mathscr{D}t}{3E_{\mathrm{tm}}^{(\mathrm{p})}} \tag{14}$$

here, $E_{\mathrm{te}}^{(\mathrm{p})} = (\mathscr{D}\sigma_{\mathrm{e}}/\mathscr{D}t)/D_{\mathrm{e}}^{(\mathrm{p})}$ and $E_{\mathrm{tm}}^{(\mathrm{p})} = (\mathscr{D}\tau_k^k/\mathscr{D}t)/D_l^{l(\mathrm{p})}$ are the plastic tangent moduli, in which $\mathscr{D}/\mathscr{D}t$ denotes the Jaumann rate. Since

$$\frac{\mathscr{D}\sigma_{\mathrm{e}}}{\mathscr{D}t} = \frac{3}{2\sigma_{\mathrm{e}}} S_k^l \frac{\mathscr{D}\tau_l^k}{\mathscr{D}t} \tag{15}$$

equation (14) can be rewritten as

$$D_j^{i(\mathrm{p})} = \frac{9}{4E_{\mathrm{te}}^{(\mathrm{p})}} \frac{S_j^i S_k^l}{\sigma_{\mathrm{e}}^2} \frac{\mathscr{D}\tau_l^k}{\mathscr{D}t} + \delta_j^i \frac{1}{3E_{\mathrm{tm}}^{(\mathrm{p})}} \frac{\mathscr{D}\tau_k^k}{\mathscr{D}t}. \tag{16}$$

Assuming that the total deformation rate is composed of an elastic part following Hooke's law and of a plastic component given in equation (16), eventually we find

$$D_j^i = D_j^{i(\mathrm{e})} + D_j^{i(\mathrm{p})}$$

$$= \frac{1}{E}\left[(1+\nu)\frac{\mathscr{D}\tau_j^i}{\mathscr{D}t} - \nu\delta_j^i \frac{\mathscr{D}\tau_k^k}{\mathscr{D}t}\right] + \frac{9}{4E_{\mathrm{te}}^{(\mathrm{p})}} \frac{S_j^i S_k^l}{\sigma_{\mathrm{e}}^2} \frac{\mathscr{D}\tau_l^k}{\mathscr{D}t} + \delta_j^i \frac{1}{3E_{\mathrm{tm}}^{(\mathrm{p})}} \frac{\mathscr{D}\tau_k^k}{\mathscr{D}t} \tag{17}$$

and its inverse form

$$\frac{\mathscr{D}\tau^{ij}}{\mathscr{D}t} = \frac{E}{(1+\nu)}\left[\tfrac{1}{2}(g^{ik}g^{jl} + g^{il}g^{jk}) + g^{ij}g^{kl}\frac{\nu - E/3E_{\mathrm{tm}}^{(\mathrm{p})}}{1 - 2\nu + E/E_{\mathrm{tm}}^{(\mathrm{p})}} - \frac{3}{2\sigma_{\mathrm{e}}^2}\frac{E}{E_{\mathrm{te}}^{(\mathrm{p})}}\frac{S^{ij}S^{kl}}{\tfrac{2}{3}(1+\nu) + E/E_{\mathrm{te}}^{(\mathrm{p})}}\right] D_{kl}. \tag{18}$$

The expression for the elastic deformation rate $D_j^{i(\mathrm{e})}$ is an inference from Hooke's law commonly used in the small strain case in which, E and ν are Young's modulus and Poisson's ratio, respectively.

Equations (17) and (18) have the same forms as the dilatational plastic constitutive equations proposed by Li and Howard [11]. The process of derivation clearly demonstrates that these equations are not dependent on a particular plastic potential nor on the so-called convexity and normality rule. They are also irrelevant to the restriction that within a stress or strain cycle the work dissipated must be positive. The basis of the derivation is an equivalent transformation between the expressions used for the rate of dissipated plastic work. Obviously this transformation form may not be unique. However, it has a kind of generality, since it implies no restrictions associated with conventional plasticity.

In the up-dated Lagrangian formulation, the difference between Kirchhoff stress and Cauchy stress, as stated in equation (2), diminishes at each of the generalized times t_0 initiated and fixed for referential configuration. Therefore the Cauchy stress will be used to represent the stress terms included in the calculation of the deviatoric stress S^{ij} or mean stress σ_{m}. We need only distinguish the use of stress definitions in the stress rates.

According to the damage situation, we shall mainly take notice of two categories for the determination of the plastic tangent moduli $E_{\mathrm{te}}^{(\mathrm{p})}$ and $E_{\mathrm{tm}}^{(\mathrm{p})}$.

Plastic strain without damage

Usually this case refers to ductile material under small straining. When $E_{\mathrm{tm}}^{(\mathrm{p})} \to \infty$, equations (17) and (18) reduce to the forms of Prandtl–Reuss relations and fall into the category where

conventional plasticity holds. Drucker's postulate and its consequences (the convexity and normality rule) can be brought into effect. If we assume that the loading surfaces have a similar shape as traced by the Von Mises yield function, then each loading surface denotes a fixed value of equivalent stress and has a one-to-one relationship with plastic equivalent strain. Consequently, the plastic tangent modulus $E_{te}^{(p)}$ can be taken as a single-valued function of $\epsilon_e^{(p)}$. To determine this function, a uniaxial stress–strain curve σ–ϵ can be employed and it is well known that

$$\frac{1}{E_{te}^{(p)}} = \frac{1}{E_t} - \frac{1}{E} \tag{19}$$

here, $E_t = d\sigma/d\epsilon$, $\sigma_e = \sigma$ (the uniaxial stress) and $\epsilon_e^{(p)} = \epsilon^{(p)}$ (the plastic part of uniaxial strain ϵ). In this case, the rules to distinguish elastic unloading from plastic loading are as stated in conventional plasticity.

Plastic strain including damage

According to microstructural modelling [4–6] and experimental studies [1–3] on void damage, it is clear and well accepted that the strain-softening effects and plastic dilatancy are the two main factors reflecting damaging behaviour. Obviously, these two factors can be incorporated into the plastic tangent moduli $E_{te}^{(p)}$ and $E_{tm}^{(p)}$. Owing to the fact that some damage occurs in shearing, e.g. shear band localization, which may not be accompanied by a substantial volumetric change, we then prefer to treat the deviatoric part and the volumetric part, separately. The crucial point is to specify the two moduli $E_{te}^{(p)}$ and $E_{tm}^{(p)}$. The specification needs to include: (a) the turning points where $E_{te}^{(p)}$ or/and $E_{tm}^{(p)}$ divert from the strain hardening state to strain-softening behaviour, (b) the determination of these two moduli as functions of stress state $\boldsymbol{\sigma}$, plastic strain state $\boldsymbol{\epsilon}^{(p)}$ and internal variables written in general form as components of vectors $\mathbf{i}_e$, $\mathbf{i}_m$ after being strain-softened; that is to say

$$E_{te}^{(p)} = f_e(\boldsymbol{\sigma}, \boldsymbol{\epsilon}^{(p)}, \mathbf{i}_e), \quad E_{tm}^{(p)} = f_m(\boldsymbol{\sigma}, \boldsymbol{\epsilon}^{(p)}, \mathbf{i}_m). \tag{20}$$

In our following computations, we again make use of the knowledge and criteria obtained from the previous microstructural studies on void damage [1–5] and propose:

(a) If either

$$\sigma_m + \lambda_e \sigma_e = \sigma_{ce} \quad \text{or} \quad \epsilon_e^{(p)} = \epsilon_{ce} \tag{21}$$

is reached, $E_{te}^{(p)}$ becomes negative. The first equation is a stress criterion, while the second one indicates that plastic equivalent strain $\epsilon_e^{(p)}$ becomes dominant in strain softening.

(b) When

$$\sigma_m + \lambda_m \sigma_e = \sigma_{cm} \tag{22}$$

then $E_{tm}^{(p)}$ also softens and becomes negative.

(c) The condition

$$\epsilon_m^{(p)} + \lambda_f \epsilon_e^{(p)} = \epsilon_c \tag{23}$$

is taken as the failure criterion. This means that, after undergoing a certain extent of strain-softening, the plastic mean strain $\epsilon_m^{(p)}$ and the equivalent strain $\epsilon_e^{(p)}$ have jointly accumulated to a critical amount, and then the material will be damaged such that it cannot carry any stress. In equations (21), (22) and (23), λ_e, σ_{ce}, ϵ_{ce}, λ_m, σ_{cm}, λ_f and ϵ_c are material constants to be determined. The three parameters λ_e, λ_m and λ_f play the role of balancing the influence between the

corresponding deviatoric and volumetric components. If $\lambda_f = 0$, the criterion of equation (23) virtually reduces to the critical void volume fraction principle used by Tvergaard[12] to switch off the elements in his finite-element computations.

In our calculations, we assume that $E_{te}^{(p)}$ and $E_{tm}^{(p)}$, after being strain-softened, are negative constants. This modelling can be modified to have a better and more sophisticated form, yet for the time being it can be taken as satisfactory in our computational implementation. Equations (21) and (22) together with the negative values assigned for $E_{te}^{(p)}$ and $E_{tm}^{(p)}$ in the strain-softening stage constitute a simple form of the functions f_e and f_m in equation (20). The constants σ_{ce} and σ_{cm} are the critical values of stress state $\boldsymbol{\sigma}$, ϵ_{ce} denotes the critical value of plastic strain state $\boldsymbol{\epsilon}^{(p)}$, while λ_e and λ_m represent the vectorial components of $\mathbf{i}_e$ and $\mathbf{i}_m$.

DETERMINATION OF THE CONSTITUTIVE PARAMETERS

In order to present a complete view of our work, a recapitulation of the previous tests [3] and computer simulations [9] needs to be included to demonstrate the determination of the constitutive parameters quoted above.

The material used for tests is a low carbon–low alloy steel. The chemical composition (% wt) is: 0.21 C, 0.25 Si, 0.66 Mn, 0.017 P, 0.010 S and 1.01 Cr. The specimens were quenched from 880°C and tempered at 710°C for 5 h. The microstructure is of a spheroidite form. The average size of inclusions is about 4 μm, while that of carbides is 0.1 μm, based on measurements taken from the photos of the scanning electron microscope.

Three types of axisymmetric bars were designed. One group is of smooth round bars with slight thinning in the middle part to initiate necking. The other two groups are specimens notched axisymmetrically with different local radii. Their basic dimensions are listed in Table 1. In which, r_0 is the minimum radius at the middle section, R_0 is the radius at the ends and R_1 denotes the local radius of the notch with B_0 as its half width. The degree of triaxial tension in the central part of the bars increases when the value of r_0/R_1 increases.

Cylindrical tension specimens (group A) and two groups of axisymmetrically notched specimens (groups B and C) were tested to measure axial load P and axial elongation ΔL. Each group contains 14 specimens. Tests on groups A and B were performed with a cross bar velocity of 1 mm/min, whilst group C was pulled at the velocity of 0.5 mm/min. Each test was terminated and unloaded at different values of elongation. The actual radii r_0 and r, referring to the smallest section of each specimen at the initial time and time of termination, respectively, were measured by an optical microscope. Thus, each specimen was pulled and stopped at a certain degree of internal damage distinguished by a necking parameter r_0/r. Five specimens were selected from each group after testing. Within each of those five specimens three $2 \times 2 \times 1$ mm small samples were cut from the central part near the narrowest section of the specimen by a line electrode spark cutting technique with their height of 1 mm along the longitudinal axis, while the 2×2 mm surface was normal to this axis. The dimensions of these samples were carefully measured under a travelling microscope

Table 1. The basic dimensions (in mm) of axisymmetric bars

Group	r_0	R_0	R_1	B_0
A	4^-	4^+	∞	
B	4.75	8	4.5	4.15
C	4.75	8	1.5	1.40

and the weight of each sample was determined by a precision balance. Using this method we easily derived the void volume fraction f_v, associated with each necking parameter at the termination of the test, from the corresponding material density γ and its initial value γ_0; since

$$f_v = (\gamma_0/\gamma) - 1. \tag{24}$$

Among the three samples of each case, the smallest density value obtained was taken as being representative, so as to avoid the local scattering influence of the material. The precision of such measurements were calibrated to have an error less than 1%.

Some basic data and figures obtained from the material test were as follows:

$$\sigma_y(\text{lower yield stress}) = 416\ \text{MPa}$$

$$\sigma_0(\text{ultimate tension strength}) = 620\ \text{MPa}.$$

and the necking parameters r_0/r at rupture were $r_0/r_f = 2.264$, 1.625 and 1.471 for groups A, B and C, respectively.

Figure 1(a) shows the relation between normalized nominal stress $P/\sigma_y A_0$ (P is the axial load and A_0 is the initial area of the smallest section) and nominal strain $\Delta L/L_0$ (L_0 is the initial length scale for measuring elongation ΔL). Based on the current radius r and area A of the smallest section at the termination of each test, we can obtain an average normalized true stress σ_s/σ_y ($=P/\sigma_y A$) and the corresponding necking parameter r_0/r. Their relations are shown in Fig. 1(b). Each data

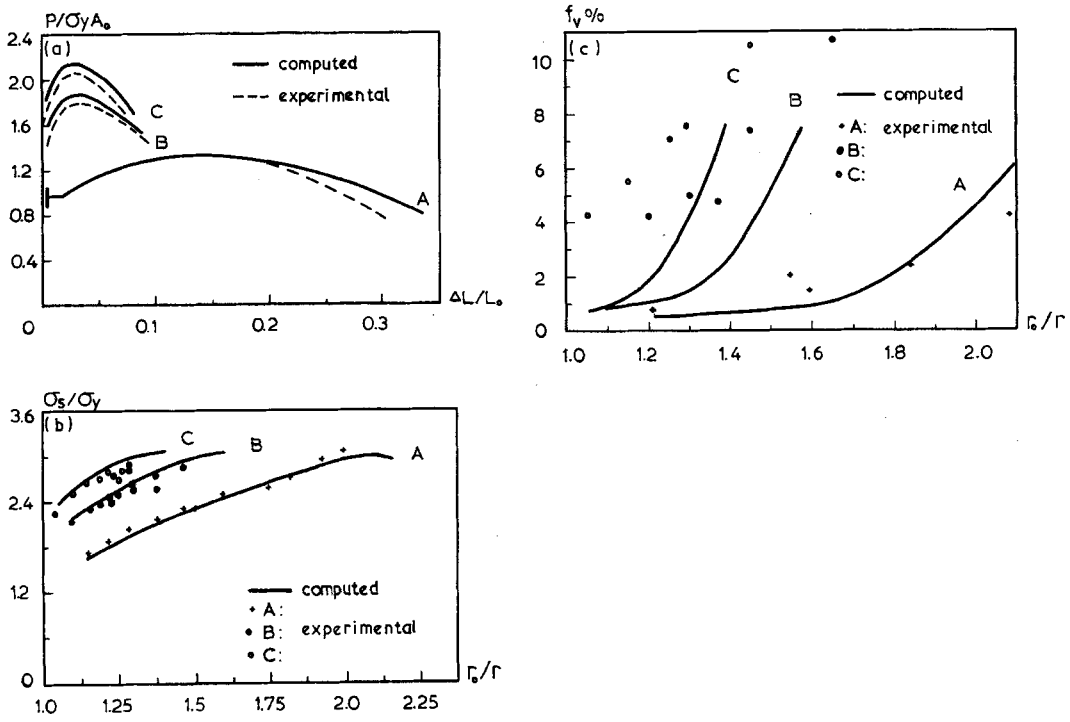

Fig. 1. Comparison of deformation characteristics via computed and experimental results for three groups of specimens (see Table 1). (a) Nominal stress $P/\sigma_y A_0$ vs nominal strain $\Delta L/L_0$, (b) average true stress σ_s/σ_y vs necking parameter r_0/r and (c) void volume fraction f_v vs necking parameter r_0/r.

point represents one terminated test. The results of the void volume fraction are depicted in Fig. 1(c). They are collected from 15 final data belonging to groups A, B and C at different stages of tension.

A large number of secondary voids were seen spreading around the primary voids, especially in group C, and they gave a bigger contribution to the total void volume fraction than the primary ones did [3]. The initiation of these tiny voids around carbides can be determined by a stress criterion, in the form of

$$\sigma_m + \lambda\sigma_e = \sigma_c \tag{25}$$

here, σ_m is the mean stress and σ_e denotes the equivalent stress, both are in the continuum sense. The material parameters, λ playing the role of a balancing factor and σ_c being the critical stress, can be determined by employing the so-called limiting curve method which had been introduced and practiced by Beremin [2] for similar use but applied to primary voids. In the case of secondary voids, we have from the tests of Xia *et al.* [3] that

$$\sigma_c = 4.6\sigma_y \quad \text{when } \lambda = 1.7.$$

Computer simulation technique in conjunction with a "trial and error" method was implemented to determine the tangent moduli $E_{te}^{(p)}, E_{tm}^{(p)}$ in equation (18) and λ_e, σ_{ce}, ϵ_{ce}, λ_m, σ_{cm}, λ_f and ϵ_c in equations (21), (22) and (23). According to a previous study of Li and Howard [13], varying the value of λ_e within a certain range has only a slight influence on the final computational result. We prefer to take

$$\lambda_e = \lambda_m = 1.7$$

so that two of the above parameters can be fixed before a computer simulation test. The essential point of the whole process is to feed in varying values for the parameters concerned in order to gain computed responses that can fit in with the experimental curves or data as close as possible. In case the error is not small enough to be taken as satisfactory, new trials should be done. As a first trial one can make use of the Bridgman formula [14]. The principle is rather easy to say yet tedious to implement. So far, to the knowledge of the authors, this is the only way of determining the material parameters from tests, instead of relying too much on void models. Although void analysis does provide valuable and even probably essential information, such as for choosing the most important internal variables, there are still many actual assumptions and neglected factors involved in the modelling [5], which definitely prevents it offering a sufficient basis for a quantitative estimation of the full effects caused by ductile damage in different materials. The inadequacies of theoretical or numerical models will be, and perhaps nowadays can only be, compensated by experimental supplements.

The final data, determined by the computer simulation technique, are listed in Table 2. We use linear interpolation between the values given in Table 2 for carrying out computations. When $\sigma_{ce}/\sigma_y = 5.3$ or $\epsilon_{ce} = 0.9$, then $E/E_{te}^{(p)} = -1000$ for the strain-softening condition in the deviatoric stress–strain space. The ratio $E/E_{tm}^{(p)} = 1.1$ for strain hardening in volumetric stress–strain space and when $\sigma_{cm}/\sigma_y = 5.5$ is reached $E/E_{tm}^{(p)} = -70$, after being strain-softened. The failure strain in equation (23) is determined as $\epsilon_c = 0.06$ with $\lambda_f = 0.035$.

Table 2. $E/E_{te}^{(p)}$ vs $\epsilon_e^{(p)}$

$\epsilon_e^{(p)}$	0.030	0.040	0.050	0.065	0.080
$E/E_{te}^{(p)}$	84	102	143	183	257
$\epsilon_e^{(p)}$	0.120	0.200	0.600	0.750	0.900
$E/E_{te}^{(p)}$	476	500	580	700	900

The computed curves produced by this set of determined parameters (including assigning $\lambda_e = \lambda_m = 1.7$ as explained previously) are compared with the experimental results in Fig. 1(a), (b) and (c). The general agreement is fairly good. Figure 1(c) shows some noticeable difference between the computational and experimental results, yet the general trend and the final responses depicted by the simulated curves are still comparable with those of the experimental records. Taking into account the wide range and the whole stage of void volume development, we can still consider the results obtained as reasonably good. The finite-element mesh used by Yang and Li[9] for the simulation only consisted of about 700 triangular constant strain elements in each axisymmetric model of groups A, B and C. Probably the gap between experimental data and the simulated curves in Fig. 1(c) could be remedied by using a finer mesh but at a greater cost of time and expenditure.

NUMERICAL ANALYSIS OF CRACK TIP BEHAVIOUR AND CRACK PROPAGATION

Based on the up-dated Lagrangian formulation and its finite-element procedure quoted previously by Li and Howard[4] and by Yang and Li[9], the constitutive descriptions given previously can be used to analyse the stress–strain distributions around a crack tip and simulate crack propagation by switching off elements that reach the failure criterion (23). Two types of specimens were chosen using the same material as the bars described previously. One is a plane-strain example employed widely as the three-point bend beam. The span of the beam is $S = 96$ mm with its height as $W = 24$ mm and a pre-existing crack length of $a = 13.1$ mm. Another sample is an axisymmetrical round bar of diameter $\phi = 16$ mm notched by a V-shape cut into a net diameter $\phi = 10$ mm. These geometrical designs together with their finite-element meshes are shown in Fig. 2(a) and (b). Some 755 triangular constant strain elements with 408 nodes are included in Fig. 2(a) for a half span of the three-point bend beam, whilst 956 elements with 509 nodes are used to discretize a quarter of the axisymmetric bar in Fig. 2(b). The length and area of the minimum elements distributed close to the crack tip or V-notch tip are designed to be the same as those used in the axisymmetric bars employed for computer simulations quoted in the previous section. Since the magnitudes of stress and strain in each element depend on the size of element, we have to follow a "consistency" principle in choosing the size scale for the elements within the most sensitive area of vital concern, so as to apply those material parameters determined previously. That is to say, the determined material parameters are associated with an implicit size scale parameter. If we change the latter, then the values of the material parameters will also change. This view reflects the fact that an absolute size scale is also one of the governing factors that influence the problem. According to our experience, we determine the size scale of the minimum element via the following considerations:

(a) Large enough to smear out the local inhomogeneity of material, so that microstructural effects can be included in a continuum modelling.
(b) Small enough to represent the drastic gradient of stress and strain near the crack tip.
(c) To implement the "consistency" principle mentioned previously, we use a $250 \times 250\ \mu$m square and subdivide it into four equal triangles as shown in the mesh parts named A in Fig. 2(a) and (b).

Figure 3(a) shows the development of plasticity in the ligament region of the beam for a different deflection of loading, Δ, at point C. Each Δ value is normalized by the height W of the beam. The plastic area first embraces the crack tip in a dumb-bell shape. Then it emerges from the top side close to the concentrated loading point. At $\Delta/W = 0.016$, the two discrete plastic areas join

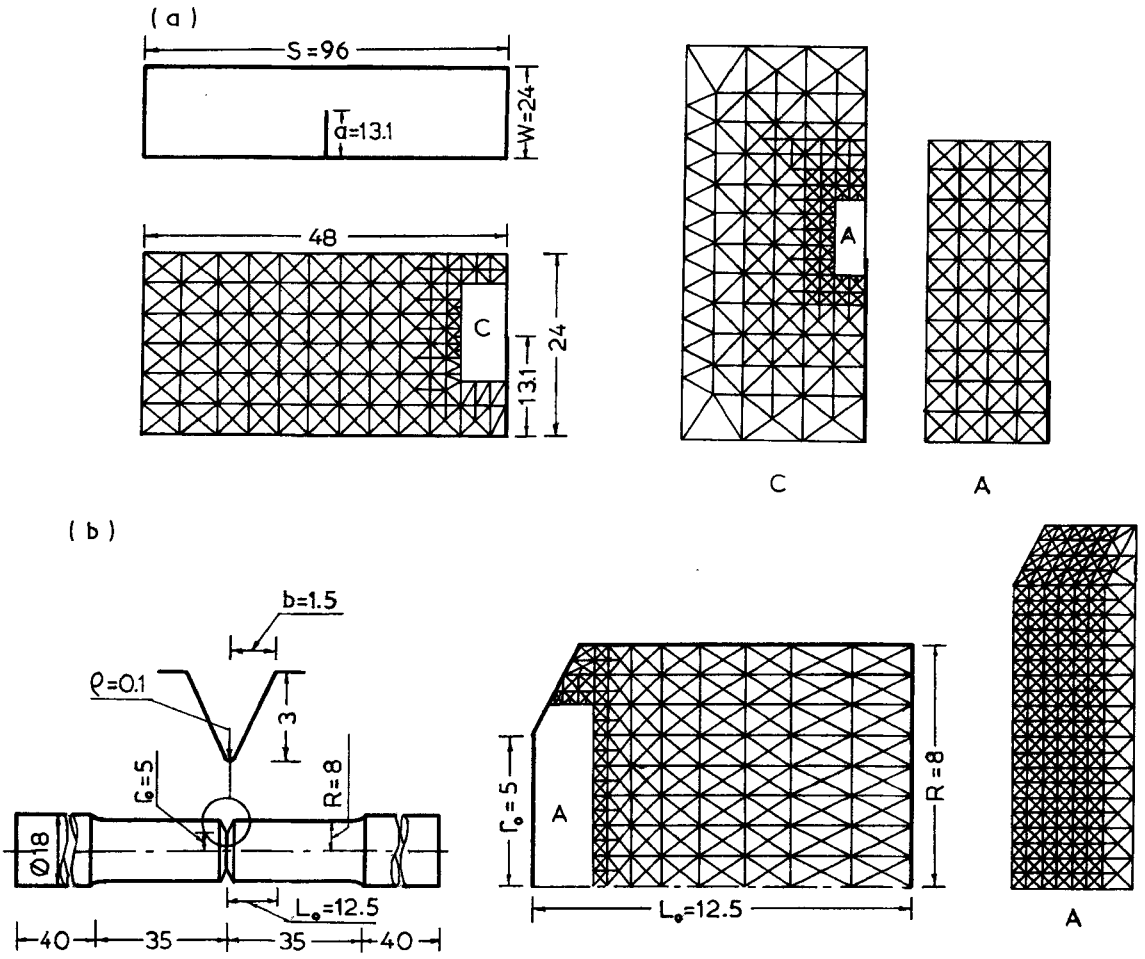

Fig. 2. Finite-element idealization (length in mm). (a) Three-point bend beam and (b) axisymmetrically notched bar.

together, yet leaving an elastic part enclosed in a round area between the crack tip and the top of the ligament section. The round area shrinks when the plastic region expands under further loading. In conjunction with the spread of the plastic area, the crack tip gradually blunts as shown in Fig. 3(b).

The total equivalent strain ϵ_e and mean strain ϵ_m are determined by conventional definitions as

$$\epsilon_e = \int_0^t D_e \, dt \quad D_e = (\tfrac{2}{3} d_j^i d_i^j)^{1/2} \quad d_j^i = D_j^i - \delta_j^i (\tfrac{1}{3} D_k^k) \quad \epsilon_m = \int_0^t D_m \, dt \quad D_m = \tfrac{1}{3} D_k^k. \tag{26}$$

The distributions of normalized stresses (equivalent stress σ_e and mean stress σ_m, both normalized by the yield stress σ_y) and of strains (equivalent strain ϵ_e and mean strain ϵ_m) near the crack tip along the centre line of the beam are shown in Fig. 4; the crack starts to propagate when Δ/W reaches about 0.055. The pictures depicted in Fig. 4 demonstrate that the distributions of stresses and strains remain almost constant during crack propagation. Since a strain-softening model is

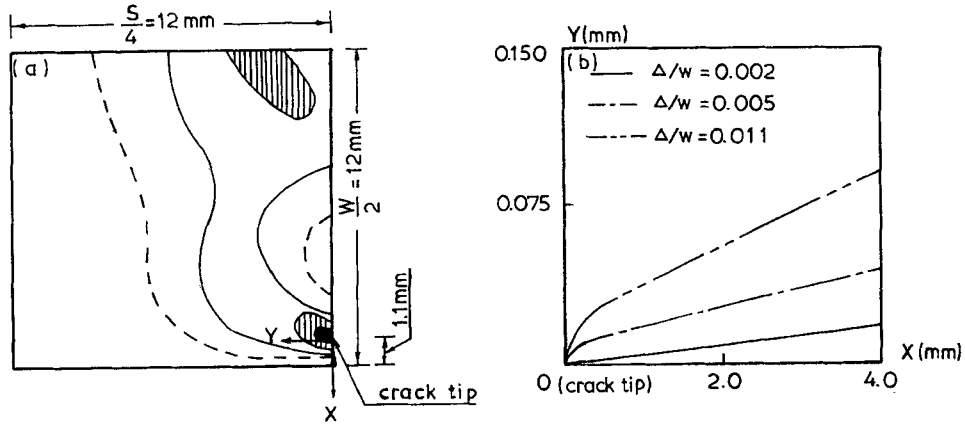

Fig. 3. Illustrations in the three-point bend beam. (a) The development of plastic area in the ligament under the normalized deflection $\Delta/W = 0.004$ (■), 0.009 (▥), 0.016 (——) and 0.055 (– – –) and (b) blunting of crack tip at $X = 0$ in the initial loading stage [the directions of X and Y are specified in Fig. 3(a)].

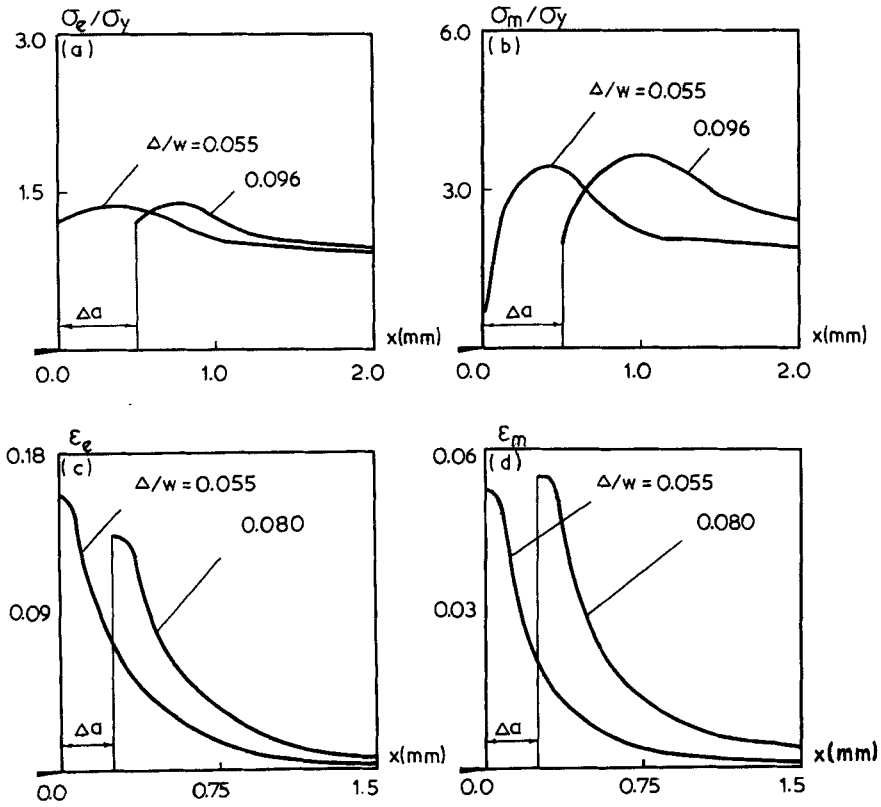

Fig. 4. Distributions of stresses (σ_e, σ_m) and strains (ϵ_e, ϵ_m) near crack tip of the beam during crack propagation.

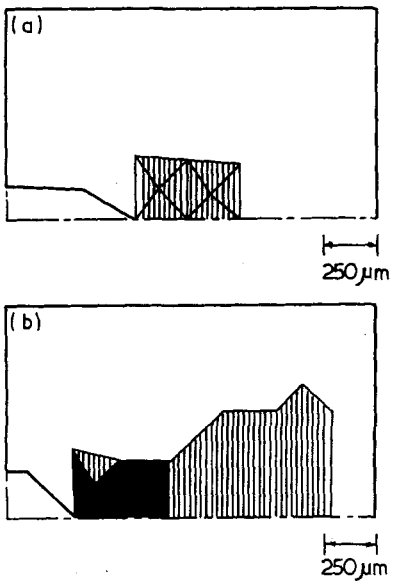

Fig. 5. Extension of strain-softened (damaged) zone (▥) and cracked material (■) in the beam. (a) $\Delta/W = 0.055$ and (b) $\Delta/W = 0.096$.

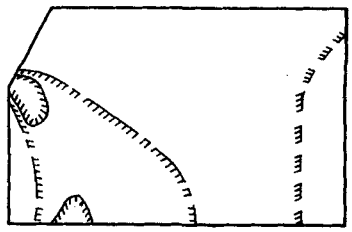

Fig. 6. The development of plastic area in the axisymmetric bar notched by a V-cut under axial elongation $\Delta L/L_0 = 0.015$ (▨), 0.052 (▨) and 0.083 (▨).

used in the computations, there is an obvious decrease in the stress distribution near the crack tip both in the deviatoric and volumetric space. At this location, strains can be highly concentrated as long as ductility permits. These features can be considered as a more realistic representation of material behaviour within the damaged zone, where the HRR field [15, 16] cannot apply. This trend is in qualitative accordance with the demonstration of Aoki *et al.*[17] using Gurson's model [6] as their basis for the constitutive equation.

The strain-softened region is very localized at the crack tip. It moves forward and widens as the crack propagates continuously. In Fig. 5, the elements hatched illustrate the area being softened (damaged), while the black (empty) elements show the crack propagation. These areas are so local, we keep their shapes edged instead of smoothed as we did for the plastic areas in Fig. 3(a).

Following the same routine, we worked on the second example of the axisymmetric bar notched by a V-cut. In Fig. 6 the plastic areas first develop separately in the wake of the notch tip and around the centre line of the bar at an elongation $\Delta L/L_0 = 0.015$. These two separate parts join and form a mushroom roof covering a convex layer of an elastic region at $\Delta L/L_0 = 0.052$. Eventually, the plastic region spreads almost throughout the bar and leaves only a disk-like boundary enclosing the last elastic volume at the top.

According to the computations, cracking initiates when $\Delta L/L_0 = 0.044$. The distributions of normalized stresses (equivalent stress σ_e and mean stress σ_m, both normalized by the yield stress σ_y) and strains (equivalent strain ϵ_e and mean strain ϵ_m) near the crack tip along the radial direction lying on the minimum section are shown in Fig. 7. Again, the wavy distributions of stresses and strains move in the direction of crack propagation. A damage zone is also seen located near the crack tip with a large accumulation of plastic strain. As illustrated in Fig. 8, this zone (marked by elements hatched) is the precursor of fracture (shown by black elements) and is restricted within a narrow region.

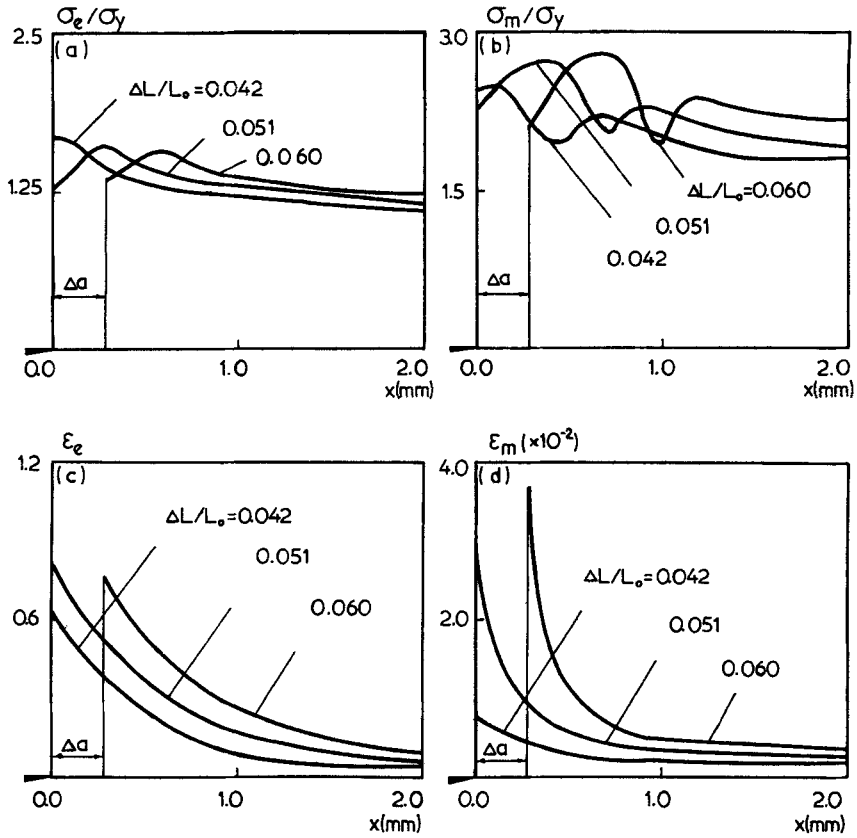

Fig. 7. Distributions of stresses (σ_e, σ_m) and strains (ϵ_e, ϵ_m) near the tip of crack in the axisymmetric bar notched by a V-cut.

Comparison between Figs 7 and 8 of this example and Figs 4 and 5 of the previous one demonstrates that, independent of the presence of a pre-existing crack, the general features of stress and strain distributions and of the cracking process are similar, and are not affected by the initial geometry of specimens. This phenomenon proves that the constitutive model proposed in this paper can correctly describe the internal damage and fracture in ductile materials, since it is based on and derived from an understanding of the effects caused by internal voids.

TESTS ON CRACK PROPAGATION IN DUCTILE MATERIAL

To validate the computations presented above, we have designed two series of tests using the same low carbon–low alloy steel.

One test was a series of three-point bend beams as shown in Fig. 2(a). Precracking was performed by a cut at the middle of the beam followed by fatigue loading. The geometrical dimensions and loading parameters of this series of tests are listed in Table 3.

In Table 3, B and W are respectively the thickness and the height of the beam and Δa denotes crack propagation with a_0 as the initial crack length and a as the crack length at the termination of each test. During testing, each beam was supported at its two ends with a fixed span

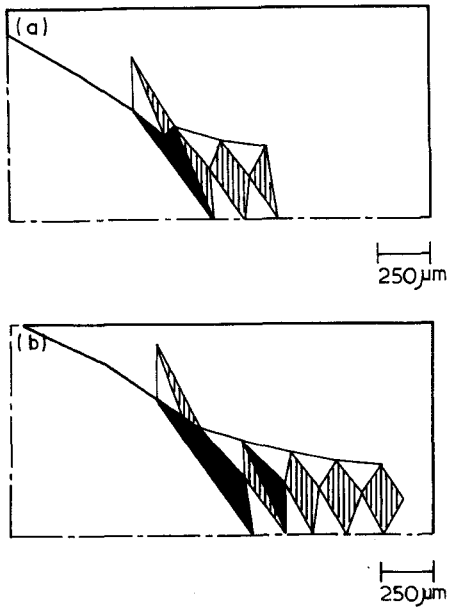

Fig. 8. The extension of the strain-softened (damaged) zone (▥) and cracked material (■) in the axisymmetric bar notched by a V-cut. (a) $\Delta L/L_0 = 0.051$ and (b) $\Delta L/L_0 = 0.065$.

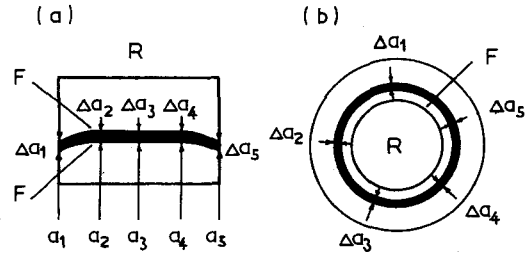

Fig. 9. Schematic demonstration for measuring (a) the initial crack length and propagation in a three-point bend beam and (b) the crack propagation in an axisymmetric bar notched by a V-cut (F: fatigue area; R: rupture area).

$S = 96.04$ mm and underwent a displacement loading at a speed of 0.5 mm/min which was stopped at the normalized deflection value Δ/W (Δ is the deflection at the middle of the beam) shown in Table 3.

Another series of tests was done with axisymmetric bars notched by V-cuts as depicted in Fig. 2(b). The bars did not have initial cracks before testing. The precise sizes with respect to the notations are marked in Fig. 2(b) and the extent of loading of each bar is given in Table 4. The local radius ρ at the sharp end of the V-cut is about 0.1 mm. Each bar is loaded under an axial displacement speed of 0.5 mm/min and stopped at an elongation $\Delta L/L_0$ shown in Table 4.

Figure 9 schematically demonstrates the method for measuring (a) the initial crack length a_0 and crack propagation Δa in the three-point bend beam, and (b) the crack propagation Δa in the axisymmetric bars notched by a V-cut. After the termination of each static loading test, the specimen underwent high frequency cycling loading to induce a fatigue crack. This mechanism delineates a clear borderline between the fatigue area and the dimpled surface caused by a ductile

Table 3. Specimens for three-point bend tests

B(mm)	W(mm)	Δ/W	a(mm)	$\Delta a/a_0$
20.02	24.03	0.048	13.38	0.0073
19.97	24.07	0.042	12.68	0.0072
19.95	24.07	0.060	12.72	0.0110
20.02	24.06	0.079	12.78	0.0161
20.03	24.07	0.074	12.32	0.0168
19.94	24.06	0.087	12.74	0.0174
20.04	24.06	0.125	10.96	0.0392
20.03	24.06	0.096	12.10	0.0245

Table 4. Axisymmetric bars with V-cut notches

R(mm)	r_0(mm)	b(mm)	$\Delta L/L_0$	$\Delta a/r_0$
8.03	5.24	1.50	0.0372	0.013
8.04	4.85	1.48	0.0469	0.045
8.03	4.99	1.50	0.0593	0.068
8.04	5.00	1.57	0.0705	0.123
8.04	5.05	1.50	0.0755	0.163

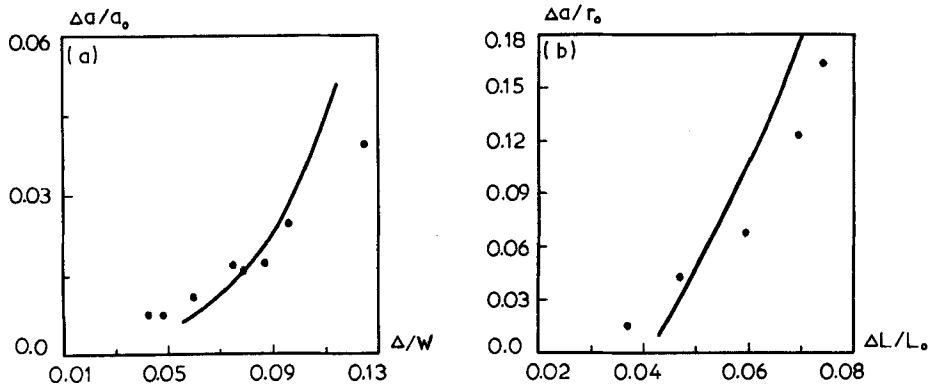

Fig. 10. Crack propagation in (a) three-point bend beams and (b) axisymmetric bars notched by a V-cut (●, experimental data, ——, computed curves).

fracture. Measurements were taken under a travelling microscope. The final value given in Tables 3 and 4 for each specimen is based on an average of five measurements as indicated in Fig. 9.

Comparison between the experimental data of crack propagation and the computed curves is shown in Fig. 10 for (a) the three-point bend beams, and (b) the axisymmetric bars notched by a V-cut. Good agreement between the test results and computational predictions can be seen. Hopefully, even better accordance would be obtained if it were able to improve the numerical simulations in Fig. 1(c) for void growth. Both Fig. 1(c) and Fig. 10 show a common trend of numerical predictions with a lower speed of void growth/crack propagation at the beginning but a faster rate by the end. Numerical simulation of cracking was implemented in our computations by employing the empty element technique suggested by Tvergaard[12]. The criterion (23) was applied to switch off very softened elements. Examples, showing the cracking process simulated by empty elements (in black) have already been illustrated in Figs 5 and 8 for the three-point bend beam and the axisymmetric bar notched by a V-cut, respectively.

CONCLUSIONS

(1) The studies introduced in this paper serve as a justification for the constitutive formulation proposed for characterizing ductile damage and fracture.

(2) The material we used has microstructural damage caused by the generations of two classes of voids. This mechanism, physically speaking, cannot be characterized by Gurson's model [6] which is based on one population of voids. Therefore the present demonstration provides another approach for examining ductile fracture problems.

(3) Computer simulation techniques in conjunction with experimental data obtained from material tests pave the way to incorporate microstructural effects and internal damage into macroscopic (continuum) constitutive formulations. Although the method has the disadvantage of tediousness in implementation, it provides a meaningful approach which takes into account physical effects hitherto neglected by other theoretical models.

(4) The considerations quoted in the paper for choosing the minimum size of finite element suggests that (if cost and time allows) a finer mesh (probably not smaller, however, than 100 μm) can be used to improve the numerical analysis.

Acknowledgements—This study was supported by the Chinese Academy of Sciences and the National Science Foundation of China.

REFERENCES

1. J. W. Hancock and M. J. Cowling (1980) Role of state of stress in crack-tip failure processes. *Met. Sci.* **14,** 293–304.
2. F. M. Beremin (1981) Cavity formation from inclusions in ductile fracture of A508 steel. *Met. Trans. A* **12A,** 723–731.
3. X. X. Xia, G. Y. Yang, Y. S. Hong and G. C. Li (1987) Tests and analysis on the ductile fracture of axisymmetric specimens. In *Mechanical Behaviour of Materials, V. Proc. ICM5,* Vol. 1, pp. 199–204, Beijing, People's Republic of China.
4. G. C. Li and I. C. Howard (1983) The effect of strain-softening in the matrix material during void growth. *J. Mech. Phys. Solids* **31,** 85–102.
5. G. C. Li, T. Guennouni and D. François (1989) Influence of secondary void damage in the matrix material around voids. *Fatigue Fract. Engng Mater. Struct.* **12,** 105–122.
6. A. L. Gurson (1977) Continuum theory of ductile rupture by void nucleation and growth: part 1—Yield criteria and flow rules for porous ductile media. *J. Engng Mater. Technol.* **99,** 2–15.
7. G. C. Li (1989) The mechanical behaviour of ductile materials damaged by two generations of voids. *Acta mech. solid. Sinica* **2,** 175–187.
8. R. Becker, A. Needleman, O. Richmond and V. Tvergaard (1988) Void growth and failure in notched bars. *J. Mech. Phys. Solids* **36,** 317–351.
9. G. Y. Yang and G. C. Li (1986) Computer simulation of the ductile fracture behaviour in axisymmetric bars. In *Computer Modelling of Fabrication Process and Constitutive Behaviour of Matals, Proc. Inter. Conf.*, pp. 385–396, Ottawa, Ontario, Canada.
10. R. Hill (1986) On constitutive inequalities for simple materials—I. *J. Mech. Phys. Solids* **16,** 229–242.
11. G. C. Li and I. C. Howard (1984) A simulation of ductile fracture in a three-point bend specimen using a softening material response. In *Advances in Fracture Research, Proc. ICF6,* Vol. 2, pp. 1191–1196 New Delhi, India.
12. V. Tvergaard (1982) Material-failure by void coalescence in localized shear band. *Int. J. Solids Struct.* **18,** 659–672.
13. G. C. Li and I. C. Howard (1983) The sensitivity of the macroscopic consequences of void growth in ductile materials to various mechanical and geometrical microparameters. *Int. J. Solids Struct.* **19,** 1089–1098.
14. P. W. Bridgman (1952) *Studies in Large Plastic Flow and Fracture*, pp. 9–37. McGraw–Hill, New York.
15. J. W. Hutchinson (1986) Singular behaviour at the end of a tensile crack in a hardening material. *J. Mech. Phys. Solids* **16,** 13–31.
16. J. R. Rice and G. F. Rosengren (1986) Plane strain deformation near a crack tip in a power-law hardening material. *J. Mech. Phys. Solids* **16,** 1–12.
17. S. Aoki, K. Kishimoto, T. Yoshida and M. Sakata (1987) A finite element study of the near crack tip deformation of a ductile material under mixed mode loading. *J. Mech. Phys. Solids* **35,** 431–455.